Supporting Information

# Strontium Influence on the Oxygen Electrocatalysis of $La_{2-x}Sr_xNiO_{4\pm\delta}$ ($0.0 \leq x_{Sr} \leq 1.0$) Thin Films

Dongkyu Lee[1], Yueh-Lin Lee[1], Alexis Grimaud[1], Wesley T. Hong[1], Michael D. Biegalski[2], Dane Morgan[3] and Yang Shao-Horn[1,*]

*[1]Electrochemical Energy Laboratory, Massachusetts Institute of Technology, 77 Massachusetts Avenue, Cambridge, Massachusetts 02139, United States*

*[2]Center for Nanophase Materials Sciences, Oak Ridge National Laboratory, Oak Ridge, Tennessee 37831, United States*

*[3]Department of Materials Science and Engineering, University of Wisconsin–Madison, Madison, Wisconsin 53706, USA*

## Supplementary Methods

**Target Synthesis.** $La_{2-x}Sr_xNiO_{4\pm\delta}$ (LSNO, $0 \leq x_{Sr} \leq 1.0$) and $Gd_{0.2}Ce_{0.8}O_2$ (GDC) were prepared by the Pechini methods.[1] $La(NO_3)_3•6H_2O$, $Sr(NO_3)_2$□ $Ni(NO_3)_2•6H_2O$, and separately $Gd(NO_3)_3$ and $Ce(NO_3)_3$ were dissolved in de-ionized water with ethylene glycol, and citric acid (Sigma-Aldrich, USA) mixture to synthesize LSNO and GDC respectively. After esterification at 100 ºC, the resin was charred at 400 ºC and then calcined at 1,000 ºC and 1,200 ºC for 12 hours in air for GDC and LSNO, respectably. Pulsed laser deposition (PLD) target pellets with 25 mm diameter were subsequently fabricated by uniaxial pressing at 50 MPa. The LSNO and GDC pellets were fully sintered at 1,400 ºC in air for 10 hours and 1,100 ºC in air for 14 hours, respectively.

**Relaxed lattice parameter determination by *in situ* HRXRD.** The Relaxed lattice parameter $\hat{a}$ and $\hat{c}$ are derived from the following equation (where $\hat{a}$ and $\hat{c}$ are the relaxed lattice parameters for the film in an unstrained state),[2-4] $\frac{(c-\hat{c})}{\hat{c}} = \frac{-2\nu(a-\hat{a})}{1-\nu \quad \hat{a}}$, assuming $\hat{a}/\hat{c}$[5] = 3.223, 3.305, 3.333, 3.339, 3.293, and 3.25 Å for $x_{Sr} = 0$, $x_{Sr} = 0.2$, $x_{Sr} = 0.4$, $x_{Sr} = 0.6$, $x_{Sr} = 0.8$, and $x_{Sr} = 1.0$, respectably at 298 K, and $\nu = 0.3$.[2-4, 6-8] The in-plane strain is given by: $\varepsilon_{cc} = \frac{(c-\hat{c})}{\hat{c}}$ and the out of plane strain by: $\varepsilon_{aa} = \frac{(a-\hat{a})}{\hat{a}}$.

**Calculation details of strain energy density.** In the LSNO thin films, the unit cell volume can be obtained by $c.a^2$. The volumetric strain are calculated using the following equation:

$$\text{Volumetric strain} = \frac{(V_{\text{constrained}} - V_{\text{relaxed}})}{V_{\text{relaxed}}}$$

In a three dimensional linear elastic solid with loads supplied by external forces, the strain energy density over entire volume can be expressed by the equation below.[9, 10]

$$\text{U (strain energy density, J m}^{-3}\text{)} = \frac{1}{2} \cdot K \cdot \left(\frac{V_{constrained} - V_{relaxed}}{V_{relaxed}}\right)^2 \quad \text{where}$$

$$\text{K (bulk modulus, GPa)} = \frac{E}{3(1-2\upsilon)}$$

Huang et al.[11] have reported that E (young's modulus) of LNO is ~ 155 GPa at room temperature and $\nu = 0.3$[2-4, 6-8] was used in this study. Then, we can determine the strain energy density for LSNO with $0.0 \leq x_{Sr} \leq 1.0$.

**Microelectrodes Fabrication.** In situ electrochemical impedance spectroscopy (EIS) measurements were conducted to probe ORR activity on geometrically well-defined LNO microelectrodes fabricated by photolithography and acid etching, where sintered porous Pt sintered onto the backside of the YSZ substrate served as the counter electrode. OCG positive photoresist (Arch Chemical Co., USA) was applied on the LNO surface and patterned using a mask aligner (Karl Süss, Germany, $\lambda = 365$ nm). The photoresist was developed using Developer 934 1:1 (Arch Chemical Co., USA) and the thin films were etched in hydrochloric acid (HCl) to remove LNO film excess and create the circular microelectrodes (diameters ~50 μm, ~100 μm, ~150 μm, and ~200 μm, exact diameter determined by optical microscopy). Before electrochemical testing, microelectrode geometry and morphology was examined by optical microscopy (Carl Zeiss, Germany) and atomic force microscopy (AFM) (Veeco, USA). AFM measurements after acid-etching of the LSNO film revealed thickness of ~ 42, ~ 64, ~ 69, ~73 nm, ~ 79 nm, and ~ 87 nm for Sr = 0, Sr = 0.2, Sr = 0.4, Sr = 0.6, Sr = 0.8, and Sr = 1.0, respectively, at 5,000 pulses.

**Electrochemical Characterization.** Fig. S7. details the equivalent circuit and corresponding Nyquist plot for this experimental system. *ZView* software (Scribner Associates, USA) was used to construct the equivalent circuit and perform complex least squares fitting. The EIS data were fitted using a standard resistor ($R_1$) for *HF* and resistors ($R_2$) in parallel with a constant phase elements ($CPE_2$) for *MF* and *LF* ($R_1$-($R_2$/$CPE_2$)-($R_{ORR}$/$CPE_{ORR}$)). Based on the $p(O_2)$ dependence of the three features, physical or chemical process with regard to each frequency range can be determined.[12-15] The *HF* feature ($10^4$ – $10^5$ Hz) was found unchanged with $p(O_2)$, and its magnitude and activation energy (~1.15 eV) were comparable to those of oxygen ion conduction in YSZ reported previously.[16] The *MF* feature ($10^3$ – $10^4$ Hz), which was found to have a $p(O_2)$ independent feature, was attributed to interfacial transport of oxygen ions between the LNO film and the GDC layer. In addition, the magnitude of its capacitance was relatively small (~$10^{-6}$ F) compared to the *LF* feature (~$10^{-3}$ F). The *LF* feature ($10^{-2}$ – $10^3$ Hz) was found to have a strong $p(O_2)$ dependence. The resistance of the *LF* feature drastically increases as oxygen partial pressure decreases. In the case of thin film samples, the magnitude of capacitance is due to the oxygen content change in the films. Therefore, the electrode oxygen surface reaction corresponds with the *LF* feature. We obtained values for $R_{ORR}$; and knowing the area of the microelectrode ($A_{electrode} = 0.25\ \pi\ d_{electrode}^2$) we can determine the ORR area specific resistance ($ASR_{ORR} = R_{ORR} \cdot A_{electrode}$). The electrical surface exchange coefficient ($k^q$), which is comparable to $k^*$,[17] was determined using the expression ,[18, 19]

$$k^q = RT / 4F^2 R_{ORR} A_{electrode} c_o \qquad (1)$$

where $R$ is the universal gas constant (8.314 J mol$^{-1}$ K$^{-1}$), $T$ is the absolute temperature, $F$ is the Faraday's constant (96,500 C mol$^{-1}$), and $c_o$ is the lattice oxygen concentration in LSNO where

$$c_o = (4+\delta)/V_m, \qquad (2)$$

$V_m$ is the molar volume of LSNO at room temperature. In this study, $c_o$ was calculated with $\delta$ extracted from previous reported values.[20, 21]

$VSC$, indicative of changes in the oxygen nonstoichiometry induced by changes in the electrical potential, can be obtained from EIS data via the expression[22]

$$VSC = [1/(A_{\text{electrode}} \bullet \text{thickness})]((R_{\text{ORR}})^{1-n}Q)^{1/n}, \qquad (3)$$

where $Q$ is the non-ideal "capacitance", and n is the non-ideality factor of $CPE$. The fitted values of n for semi-circle $CPE_{\text{ORR}}$ were found to range from ~ 0.96 to 1.0 over the entire $p\text{O}_2$ range examined (n =1, ideal).

**Experimental details of *ex situ* AES.** In AES, the obtained energy spectrum for a particular element is always situated on a large background (low signal-to-noise ratio), which arises from the vast number of so-called secondary electrons generated by a multitude of inelastic scattering processes. To obtain better sensitivity for detection of the elemental peak positions, the AES spectra from this study are presented in the differentiated form. Elemental quantification of AES spectra utilized relative sensitivity factors (RSFs) of 0.059, 0.027, 0.227, and 0.212 for $\text{La}_{\text{MNN}}$, $\text{Sr}_{\text{LMM}}$, $\text{Ni}_{\text{LMM}}$, and $\text{O}_{\text{KLL}}$, respectively, as supplied by the AES manufacturer (Physical Electronics). In addition, the Inelastic-Mean-Free-Path (IMFP) was calculated to correct signal intensity for their different IMFPs (information depth). IMFPs were calculated using the NIST Standard Reference Database 71 "NIST Electron Inelastic- Mean-Free-Path Database" version 1.2. The software program provides the ability to predict the IMFP for inorganic compounds supplying the stoichiometric composition of $La_{2-x}Sr_xNiO_{4\pm\delta}$ ($0 \leq x \leq 1.0$), the number of valence electrons per molecule (assumed to be 40) and a band gap energy (for which we are assuming 0 eV as LSNO is metallic like at high temperatures; additionally when assuming a band gap of an insulator 5 eV, the IMFP increases by ~0.03 nm). The IMFP for La, Sr, and Ni were determined to be 1.361 ~ 1.395 nm, 2.611 ~ 2.667 nm, and 1.562 ~ 1.607 nm, respectively. A relative depth-scaling factor (□) was determined as:

$$\sigma_i = \int_0^{\lambda_{La}} \frac{1}{\lambda_i} \exp\left(-\frac{x}{\lambda_i}\right) dx \,, \tag{4}$$

where $\lambda_i$ is the IMFP, yielding $\sigma_{\mathrm{Ni}} = 0.58$, $\sigma_{\mathrm{Sr}} = 0.41$, and $\sigma_{\mathrm{La}} = 0.63$. The intensities from different elements were scaled using $I_{\mathrm{scaled}} = I_{\mathrm{measured}}$*□$_i$/$S_i$.

**Details of density functional theory (DFT) calculations.** Spin-polarized Density Functional Theory (DFT) calculations were preformed with the Vienna *Ab-initio* Simulation Package[23, 24] using the Projector-Augmented plane-Wave method[25] with a cutoff energy of 450 eV. Exchange-correlation was treated in the Perdew-Wang-91[26] Generalized Gradient Approximation (GGA) using the soft O_s oxygen pseudopotential. The GGA+$U$ calculations[27] are performed with the simplified spherically averaged approach[28], where the $U_{eff}$ ($U_{eff}$ = Coulomb $U$ - exchange $J$) is applied to $d$ electrons ($U_{\mathrm{eff}}$(Ni) = 6.4 eV). All calculations are performed in the ferromagnetic state in order to use a consistent and tractable set of magnetic structures.

Fully relaxed bulk LSNO (Sr content : x=0, 0.5, and 1) calculations are performed using the $2a_{tetra} \times 2a_{tetra} \times c_{tetra}$ supercells with 3×3×2 kpoints. The Sr in the LSNO bulk is arranged to have the farthest Sr-Sr pair distance in the simulated supercells. Based on the LSNO bulk configurations, the LSNO $(001)_{\text{tetra.}}$ and $(100)_{\text{tetra.}}$ surface energy and surface oxygen adsorption energy are calculated using $2a_{tetra}\times 2\ a_{tetra}$ 9-layer (001) and $2a_{tetra}\times\ c_{tetra}$ 6-layer $(100)_{\text{tetra.}}$ slabs in periodic boundary conditions with 10 Å vacuum between the two surfaces, as illustrated in Fig. S9 (the kpoints setups are: 3×3×1 kpoints for the 9-layer $(001)_{\text{tetra.}}$ slab and 1×3×2 kpoints for the 6-layer $(100)_{\text{tetra.}}$ slab).

The surface energies ($E_{surf}$) are then obtained using the equation below:

$$E_{surf} = \tfrac{1}{2}\,(E_{slab} - N \bullet E_{bulk})/A_{surf} \qquad (5)$$

where $E_{slab}$ is the calculated total energy of LSNO slabs, $E_{bulk}$ is the calculated total energy of LSNO bulk normalized as per formula unit, $N$ is the number of LSNO units in the slab, and $A_{surf}$ is the surface area of the simulated slabs.

Oxygen adsorption energies ($E_{ads}$) are calculated based on the following equation:

$$E_{ads} = E_{O\text{-}adsorbed\text{-}slab} - E_{slab} - \tfrac{1}{2} \bullet E_{O2} \qquad (6)$$

where $E_{O\text{-}adsorbed\text{-}slab}$ is the calculated total energy of LSNO slabs with a surface adsorbed oxygen at the adsorption site illustrated in Fig. S8 (c and d), and $E_{O2}$ is the calculated total energy of isolated $O_2$ molecule corrected with +0.33 eV/O, which is obtained by fitting to a series of binary oxide experimental formation enthalpies at room temperature.[29]

Finally, we distinguished that the $(100)_{\text{tetra.}}$ orientation in this work is equivalent to the defined $(110)_{\text{tetra.}}$ orientation in the previous theoretical study done by Read et al.[30] Our calculated surface energy based on the $(100)_{\text{tetra.}}$ surface configuration suggested by Read et al.[30] (in Figure 1(a) and Figure 3 of Ref. 30) at $x_{Sr}$=0, 0.5, and 1 is found to be less stable (surface energy range between 0.09~0.10 eV/A$^2$) than the two main surfaces investigated in this work (between 0.06~0.08 eV/A$^2$, see Fig. 3a of the main content), due to that the alternating $O_2$ (layer charge of -4) and $A_2BO_2$ (layer charge of +4) layers give rise to polar instability.[31] Nonetheless, the relative surface stability of $(110)_{tetra.}$ vs. $(001)_{tetra.}$ and Sr solution energy reported by Read et al.[30], which is equivalent to the $(100)_{tetra.}$ and $(001)_{tetra.}$ surfaces in this work, is consistent with the calculated surface energetics in our DFT simulations.

## References

1. M. Pechini, *U.S. Patent No. 3,330,697*, 1967.
2. H. M. Christen, E. D. Specht, S. S. Silliman and K. S. Harshavardhan, *Phys. Rev. B*, 2003, **68**, 4.
3. E. J. Crumlin, E. Mutoro, Z. Liu, M. E. Grass, M. D. Biegalski, Y. L. Lee, D. Morgan, H. M. Christen, H. Bluhm and Y. Shao-Horn, *Energy Environ. Sci.*, 2012, **5**, 6081-6088.
4. G. J. la O, S. J. Ahn, E. Crumlin, Y. Orikasa, M. D. Biegalski, H. M. Christen and Y. Shao-Horn, *Angew. Chem.-Int. Edit.*, 2010, **49**, 5344-5347.
5. J. Gopalakrishnan, G. Colsmann and B. Reuter, *J. Solid State Chem.*, 1977, **22**, 145-149.
6. E. J. Crumlin, E. Mutoro, S. J. Ahn, G. J. la O, D. N. Leonard, A. Borisevich, M. D. Biegalski, H. M. Christen and Y. Shao-Horn, *J. Phys. Chem. Lett.*, 2010, **1**, 3149-3155.
7. D. Lee, A. Grimaud, E. J. Crumlin, K. Mezghani, M. A. Habib, Z. Feng, W. T. Hong, M. D. Biegalski, H. M. Christen and Y. Shao-Horn, *The Journal of Physical Chemistry C*, 2013, **117**, 18789-18795.

8. D. Y. Noh, Y. Hwu, J. H. Je, M. Hong and J. P. Mannaerts, *Appl. Phys. Lett.*, 1996, **68**, 1528-1530.

9. U. C. Jindal, *Strength of Materials*, Pearson Education India, 2012.

10. A. F. Bower, *Applied mechanics of solids*, CRC Press, 6000 Broken Sound Parkway NW, suite 300, Boca Raton, FL 33487, 2009.

11. B. X. Huang, J. Malzbender and R. W. Steinbrech, *J. Mater. Sci.*, 2011, **46**, 4937-4941.

12. S. B. Adler, *Chem. Rev.*, 2004, **104**, 4791-4843.

13. S. B. Adler, J. A. Lane and B. C. H. Steele, *J. Electrochem. Soc.*, 1996, **143**, 3554-3564.

14. T. Kawada, J. Suzuki, M. Sase, A. Kaimai, K. Yashiro, Y. Nigara, J. Mizusaki, K. Kawamura and H. Yugami, *J. Electrochem. Soc.*, 2002, **149**, E252-E259.

15. Y. L. Yang, C. L. Chen, S. Y. Chen, C. W. Chu and A. J. Jacobson, *J. Electrochem. Soc.*, 2000, **147**, 4001-4007.

16. P. S. Manning, J. D. Sirman, R. A. DeSouza and J. A. Kilner, *Solid State Ion.*, 1997, **100**, 1-10.

17. J. Maier, *Solid State Ionics*, 1998, **112**, 197-228.

18. J. Maier, *Physical Chemistry of Ionic Materials: Ions and Electrons in Solids* John Wiley, Chichester, England ; Hoboken, NJ, 2004.

19. J. Fleig and J. Maier, *J. Eur. Ceram. Soc.*, 2004, **24**, 1343-1347.

20. T. Nakamura, K. Yashiro, K. Sato and J. Mizusaki, *Phys. Chem. Chem. Phys.*, 2009, **11**, 3055-3062.

21. V. V. Vashook, H. Ullmann, O. P. Olshevskaya, V. P. Kulik, V. E. Lukashevich and L. V. Kokhanovskij, *Solid State Ion.*, 2000, **138**, 99-104.

22. J. Fleig, *Solid State Ion.*, 2002, **150**, 181-193.

23. G. Kresse and J. Furthmuller, *Phys. Rev. B*, 1996, **54**, 11169-11186.

24. G. Kresse and J. Hafner, *Phys. Rev. B*, 1993, **47**, 558-561.

25. P. E. Blochl, *Phys. Rev. B*, 1994, **50**, 17953-17979.

26. J. P. Perdew and Y. Wang, *Physical Review B*, 1992, **45**, 13244.

27. V. I. Anisimov, F. Aryasetiawan and A. I. Lichtenstein, *Journal of Physics-Condensed Matter*, 1997, **9**, 767-808.

28. S. L. Dudarev, G. A. Botton, S. Y. Savrasov, C. J. Humphreys and A. P. Sutton, *Phys. Rev. B*, 1998, **57**, 1505-1509.

29. Y. L. Lee, J. Kleis, J. Rossmeisl and D. Morgan, *Phys. Rev. B*, 2009, **80**.

30. M. S. D. Read, M. S. Islam, G. W. Watson and F. E. Hancock, *J. Mater. Chem.*, 2001, **11**, 2597-2602.

31. J. Goniakowski, F. Finocchi and C. Noguera, *Rep. Prog. Phys.*, 2008, **71**.

32. M. Burriel, G. Garcia, J. Santiso, J. A. Kilner, J. C. C. Richard and S. J. Skinner, *J. Mater. Chem.*, 2008, **18**, 416-422.

33. A. Yamada, Y. Suzuki, K. Saka, M. Uehara, D. Mori, R. Kanno, T. Kiguchi, F. Mauvy and J. C. Grenier, *Adv. Mater.*, 2008, **20**, 4124-+.

34. M. Yashima, S. Sasaki, M. Kakihana, Y. Yamaguchi, H. Arashi and M. Yoshimura, *Acta Crystallogr. Sect. B-Struct. Commun.*, 1994, **50**, 663-672.

35. B. Matovic, S. Boskovic, L. Zivkovic, M. Vlajic and V. Krstic, in *Current Research in Advanced Materials and Processes*, eds. D. P. Uskokovic, S. K. Milonjic and D. I. Rakovic, Trans Tech Publications Ltd, Zurich-Uetikon, Editon edn., 2005, vol. 494, pp. 175-179.

Table S1. Lattice mismatch between the film materials and the substrate materials.

| Materials (bulk) | $\boldsymbol{a}_{\text{bulk}}$ /Å | $\boldsymbol{c}_{\text{bulk}}$ / Å | Substrate / Å | Lattice mismatch (***a-b*** plane) | Lattice mismatch (***c*** plane) |
|---|---|---|---|---|---|
| $La_{2-x}Sr_xNiO_{4\pm\delta}$, x=0[5] | 3.881 | 12.51 | $SrTiO_3$ (100), $\boldsymbol{a}_{\text{STO}}$ = 3.906[32] | ~ -0.6 % | ~ 6.76 % |
| | | | $NdGaO_3$ (110), $\boldsymbol{a}_{\text{NGO}}$= 3.863[32] | ~ 0.47 % | ~ 7.95 % |
| $Nd_2NiO_{4+\delta}$[33] | 3.854 | 12.214 | YSZ (001), $\boldsymbol{a}_{\text{YSZ}}$ = 5.147[34] | ~ 6.9 % | ~ 11.9 % |
| $La_{2-x}Sr_xNiO_{4\pm\delta}$, x=0 | 3.881 | 12.51 | GDC (001), $\boldsymbol{a}_{\text{GDC}}$= 5.418[35] | ~ 1.3% | ~ 8.8 % |
| | | | YSZ (001), $\boldsymbol{a}_{\text{YSZ}}$= 5.147 | ~ 6.7 % | ~ 14.6 % |
| $La_{2-x}Sr_xNiO_{4\pm\delta}$, x=0.2[5] | 3.842 | 12.70 | GDC (001), $\boldsymbol{a}_{\text{GDC}}$= 5.418 | ~ 0.3 % | ~ 10.5 % |
| | | | YSZ (001), $\boldsymbol{a}_{\text{YSZ}}$= 5.147 | ~ 5.6 % | ~ 16.3 % |
| $La_{2-x}Sr_xNiO_{4\pm\delta}$, x=0.4[5] | 3.819 | 12.72 | GDC (001), $\boldsymbol{a}_{\text{GDC}}$= 5.418 | ~ - 0.3 % | ~10.8 % |
| | | | YSZ (001), $\boldsymbol{a}_{\text{YSZ}}$= 5.147 | ~ 4.9 % | ~ 16.6 % |
| $La_{2-x}Sr_xNiO_{4\pm\delta}$, x=0.6[5] | 3.807 | 12.722 | GDC (001), $\boldsymbol{a}_{\text{GDC}}$= 5.418 | ~ - 0.6 % | ~ 10.6 % |
| | | | YSZ (001), $\boldsymbol{a}_{\text{YSZ}}$= 5.147 | ~ 4.6 % | ~ 16.4 % |
| $La_{2-x}Sr_xNiO_{4\pm\delta}$, x=0.8[5] | 3.814 | 12.559 | GDC (001), $\boldsymbol{a}_{\text{GDC}}$= 5.418 | ~ - 0.4 % | ~ 9.3 % |
| | | | YSZ (001), $\boldsymbol{a}_{\text{YSZ}}$= 5.147 | ~ 4.8 % | ~ 15 % |

| | | | | | |
|---|---|---|---|---|---|
| $La_{2-x}Sr_xNiO_{4\pm\delta}$, x=1.0[5] | 3.824 | 12.429 | GDC (001), $\boldsymbol{a}_{GDC}$= 5.418 | ~ - 0.2 % | ~ 8.1 % |
| | | | YSZ (001), $\boldsymbol{a}_{YSZ}$ = 5.147 | ~ 5.1 % | ~ 13.8 % |

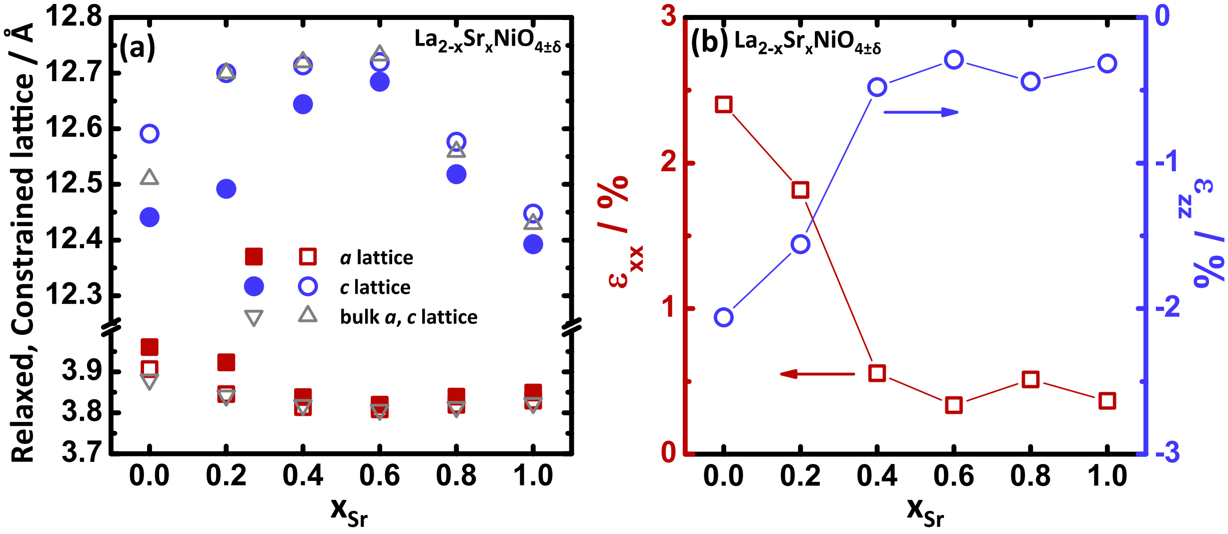

Fig. S1: (a) Constrained (■-red, ●-blue) and Relaxed (□-red, ○-blue) lattice parameters of the $La_{2-x}Sr_xNiO_{4\pm\delta}$ (LSNO) thin films as a function of Sr content at room temperature. Extrapolated bulk $\boldsymbol{a}_{tetra.}$ (▽-gray) and $\boldsymbol{c}_{tetra.}$ (△-gray) lattice parameters at room temperature obtained from previous data of Gopalakrishanan et al.[5] are plotted for comparison. The constrained normal and in-plane lattice parameters of the LSNO films were calculated from combining the interplanar distances of the $(200)_{tetra.}$, $(103)_{tetra.}$ and $(006)_{tetra.}$ peaks. (b) Out of plane and in-plain strain as a function of the Sr content calculated using $\varepsilon_{xx} = \frac{(c-\hat{c})}{\hat{c}}$ and $\varepsilon_{zz} = \frac{(a-\hat{a})}{\hat{a}}$ for in-plane strain and out of plane strain respectably. For determining the relaxed film lattice parameter $\hat{\boldsymbol{a}}$ and $\hat{\boldsymbol{c}}$, we used the equation:

$\frac{(c-\hat{c})}{\hat{c}} = \frac{-2\nu}{1-\nu}\frac{(a-\hat{a})}{\hat{a}}$, assuming $\hat{\boldsymbol{a}}/\hat{\boldsymbol{c}}$[5] = 3.223, 3.305, 3.333, 3.339, 3.293, and 3.25 Å for $x_{Sr} = 0$, $x_{Sr} = 0.2$, $x_{Sr} = 0.4$, $x_{Sr} = 0.6$, $x_{Sr} = 0.8$, and $x_{Sr} = 1.0$, respectably at 298 K, and $\nu = 0.3$.

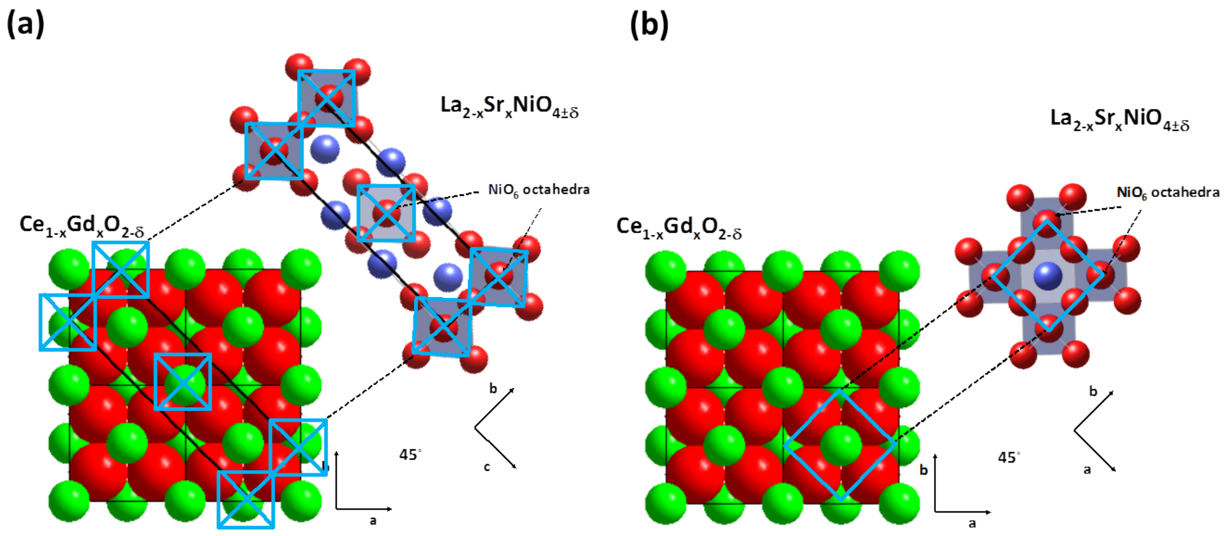

Fig. S2: Schematic of two different orientations of $La_{2-x}Sr_xNiO_{4\pm\delta}$ (LSNO) on GDC (a) $(100)_{tetra.}$-oriented epitaxial LSNO thin film and (b) $(001)_{tetra.}$-oriented epitaxial LSNO thin films.

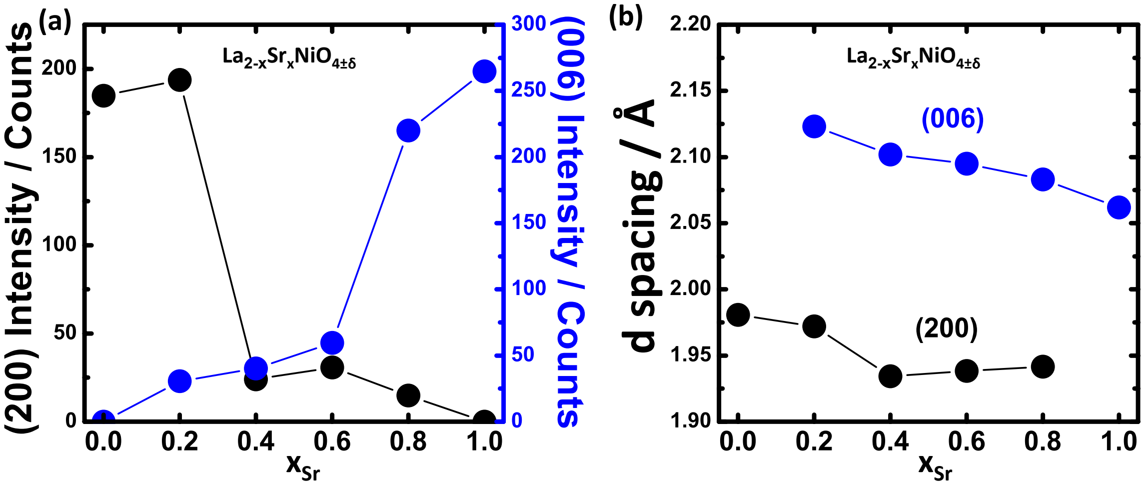

Fig. S3: (a) Peak intensities and (b) d spacing of the $La_{2-x}Sr_xNiO_{4\pm\delta}$ (LSNO) thin film $(006)_{tetra.}$ and $(200)_{tetra.}$ as a function of Sr content obtained from HRXRD. The peak intensities of $(200)_{tetra.}$ significantly decreases with increasing the Sr content while those of $(006)_{tetra.}$ significantly increases, which suggests that once $(00l)_{tetra.}$ orientation growth begins, $(l00)_{tetra.}$ orientation growth is suppressed.

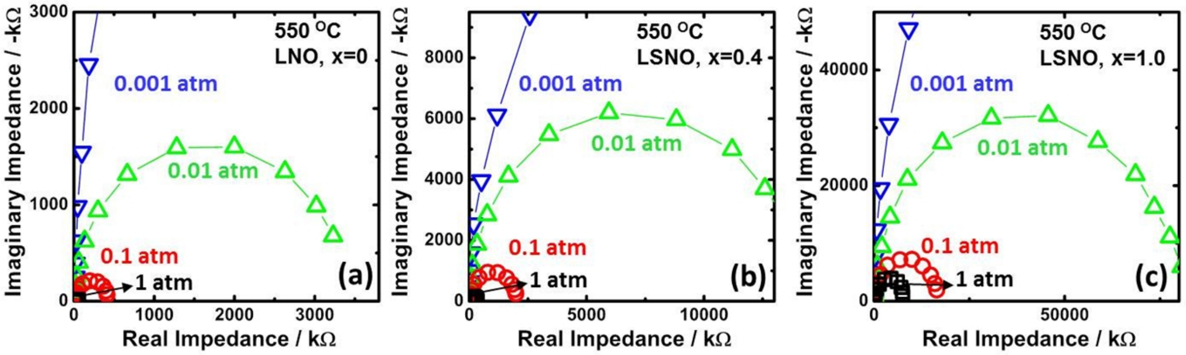

Fig. S4: Electrochemical impedance spectroscopy (EIS) results of microelectrodes for the $La_{2-x}Sr_xNiO_{4\pm\delta}$ (LSNO) thin films with $0 \le x_{Sr} \le 1.0$ at 550 $^{O}$C (a) Nyquist plot of the LNO thin film with x=0, (b) Nyquist plot of the LSNO thin film with $x_{Sr}$ = 0.4, and (c) Nyquist plot of the LSNO thin film with $x_{Sr}$ = 1.0 as a function of $p(O_2)$. All films exhibited nearly perfect predominant semicircle impedances, which indicates that the surface oxygen exchange kinetics governs the oxygen electrocatalysis on the thin film surface.[12]

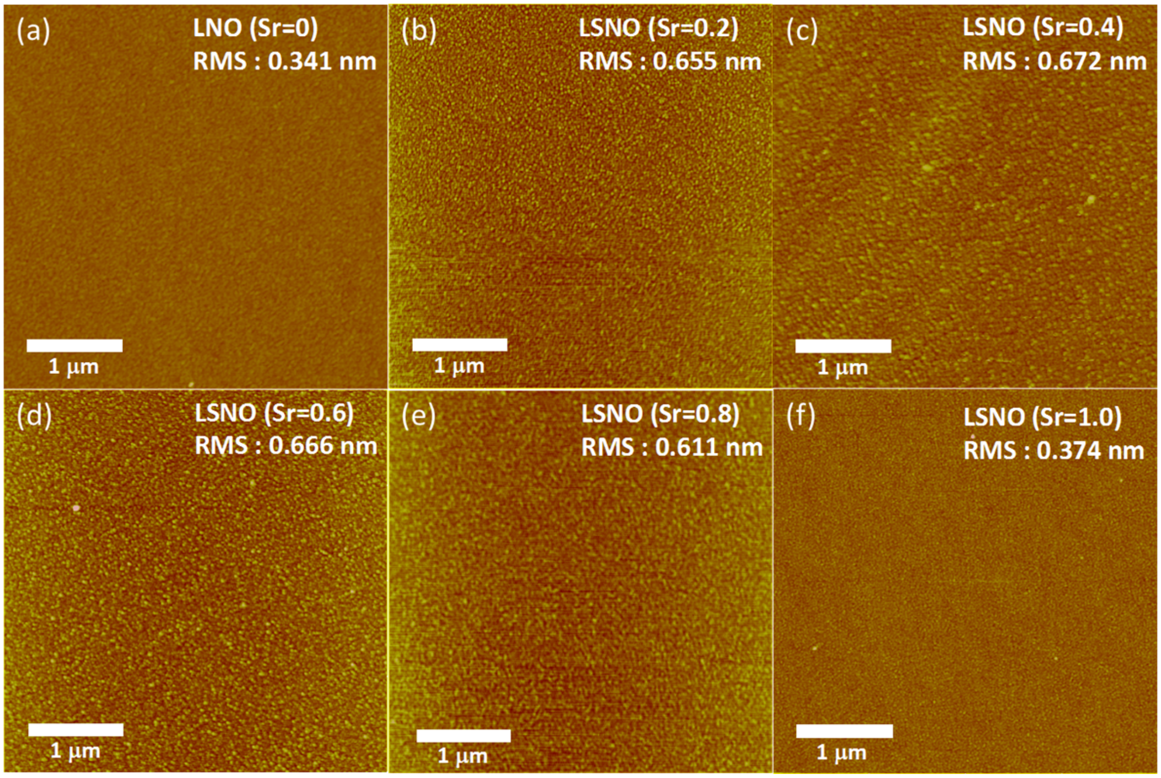

Fig. S5: AFM measurements of the as-prepared $La_{2-x}Sr_xNiO_{4\pm\delta}$ (LSNO) thin films with $0 \leq x_{Sr} \leq 1.0$ deposited at 5,000 pulses (a) $x_{Sr} = 0$ with RMS of 0.341 nm, (b) $x_{Sr} = 0.2$ with RMS of 0.655 nm, (c) $x_{Sr} = 0.4$ with RMS of of 0.672 nm, and (d) $x_{Sr} = 0.6$ with RMS of of 0.666 nm, (e) $x_{Sr} = 0.8$ with RMS of 0.611 nm, and (f) $x_{Sr} = 1.0$ with RMS of 0.374 nm.

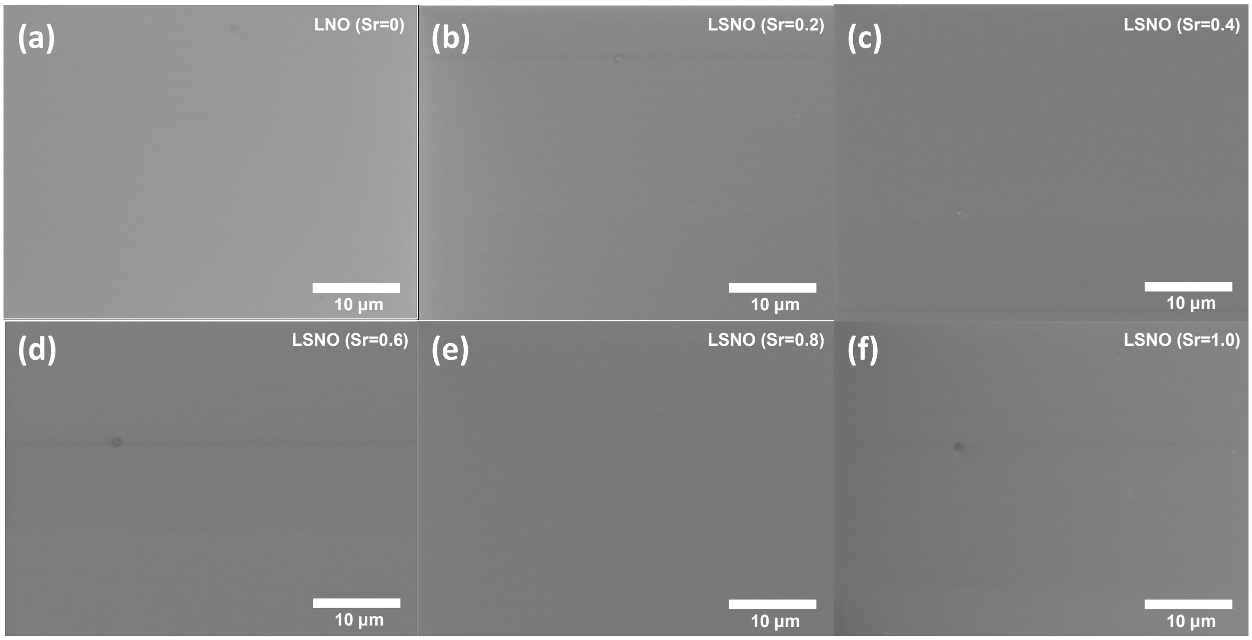

Fig. S6: Scanning electron microscopy (SEM) images of (a) $La_2NiO_{4+\delta}$ (LNO) films, (b) $La_{2-x}Sr_xNiO_{4\pm\delta}$ (LSNO) films with $x_{Sr} = 0.2$, (c) LSNO films with $x_{Sr} = 0.4$, (d) LSNO films with $x_{Sr} = 0.6$, (e) LSNO films with $x_{Sr} = 0.8$, and (f) LSNO films with $x_{Sr} = 1.0$ annealed at 550 $^{o}$C in an oxygen partial pressure of 1 atm for 6 hours.

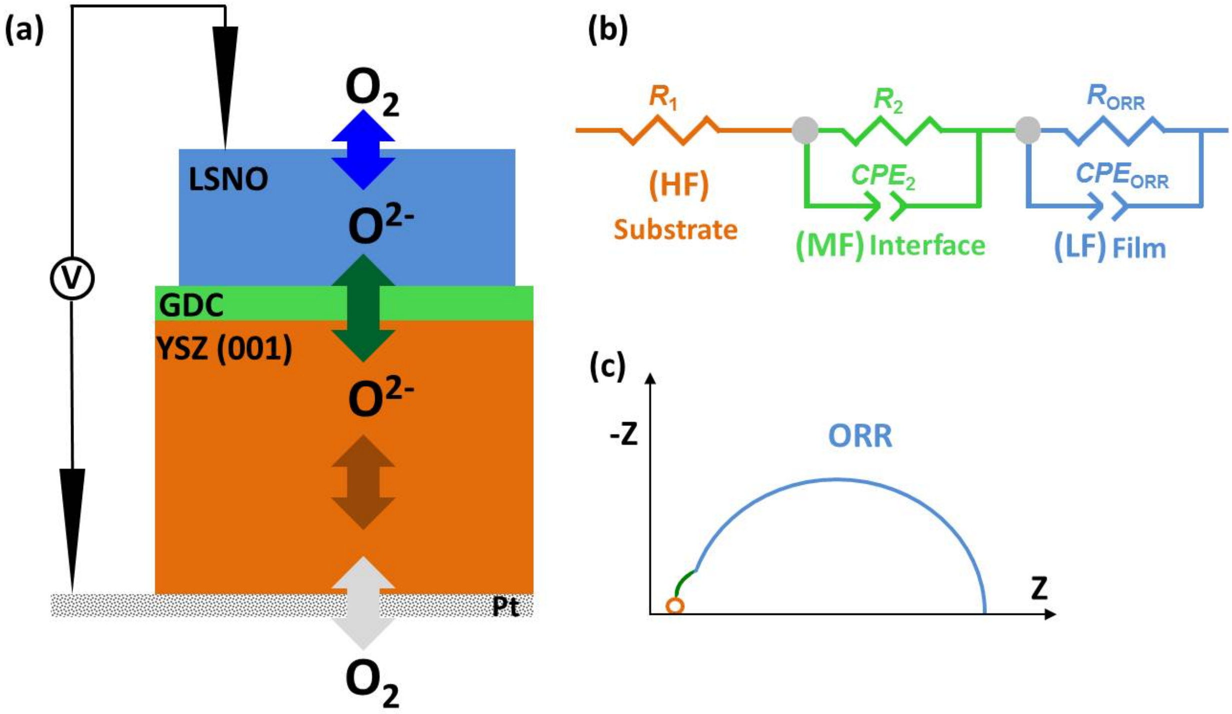

Fig. S7: (a) Schematic of a LSNO/GDC/YSZ(001)/porous Pt samples and electrochemical testing configuration (not drawn to scale), and (b) equivalent circuit ($R_1$ = YSZ electrolyte resistance, $R_2$ = electrode/electrolyte interface resistance[4], $R_{\mathrm{ORR}}$ = ORR resistance, CPE = constant phase element) used to extract ORR kinetics, and (c) characteristic Nyquist plot schematic (color key : orange = YSZ/bulk transport, green = GDC/interface, blue = LSNO/ORR).

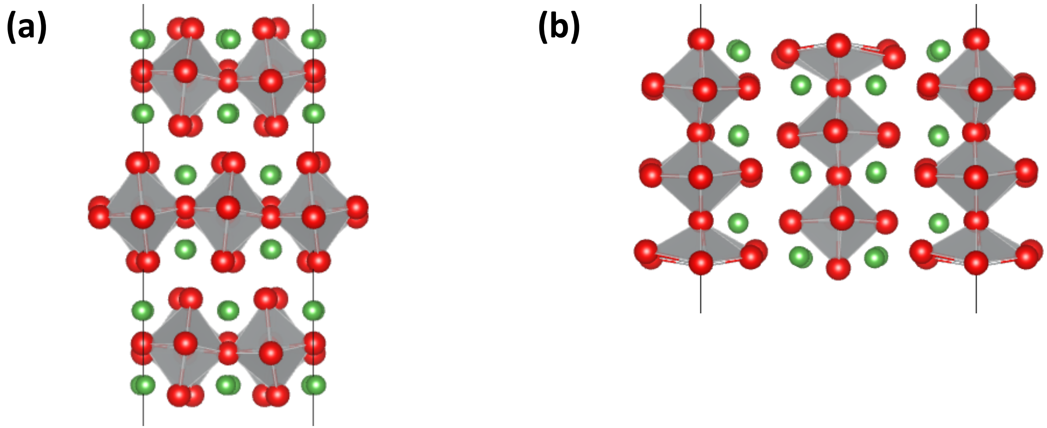

$(001)_{\text{tetra.}}$ slab – side view

$(100)_{\text{tetra.}}$ slab – side view

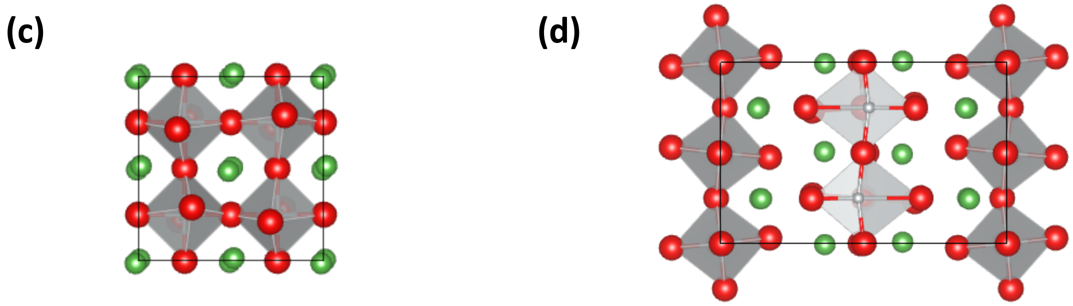

Top 3 layers of the $(001)_{\text{tetra.}}$ slab – top view

Top 3 layers of the $(100)_{\text{tetra.}}$ slab – top view

Fig. S8: Simulated $La_{2-x}Sr_xNiO_{4\pm\delta}$ (LSNO) slab models in the density functional theory calculations in this work: (a) side view of the $(001)_{\text{tetra.}}$ slab, (b) side view of the $(100)_{\text{tetra.}}$ slab, (c) top view of the top 3 layers of the $(001)_{\text{tetra.}}$ slab, and (d) top view of the top 3 layers of the $(100)_{\text{tetra.}}$ slab. The dotted circles in c and d represent the surface oxygen adsorption sites for the $(001)_{\text{tetra.}}$ and $(100)_{\text{tetra.}}$ surfaces, respectively.